

# Ctrl-V: Higher Fidelity Video Generation with Bounding-Box Controlled Object Motion

**Ge Ya Luo**

Mila, Université de Montréal  
olga.xu@umontreal.ca

**Zhi Hao Luo**

Mila, Polytechnique Montreal  
luozhiha@mila.quebec

**Anthony Gosselin**

Mila, Polytechnique Montreal  
anthony.gosselin@mila.quebec

**Alexia Jolicoeur-Martineau**

Mila, McGill University  
alexia.jolicoeur-martineau@mail.mcgill.ca

**Christopher Pal**

Mila, Polytechnique Montreal  
Canada CIFAR AI Chair

**Abstract:** With recent advances in video prediction, controllable video generation has been attracting more attention. Generating high fidelity videos according to simple and flexible conditioning is of particular interest. To this end, we propose a controllable video generation model using pixel level renderings of 2D or 3D bounding boxes as conditioning. In addition, we also create a bounding box predictor that, given the initial and ending frames' bounding boxes, can predict up to 15 bounding boxes per frame for all the frames in a 25-frame clip. We perform experiments across 3 well-known AV video datasets: KITTI, Virtual-KITTI 2 and BDD100k.

**Project page:** <https://00oolga.github.io/ctrl-v.github.io/>.

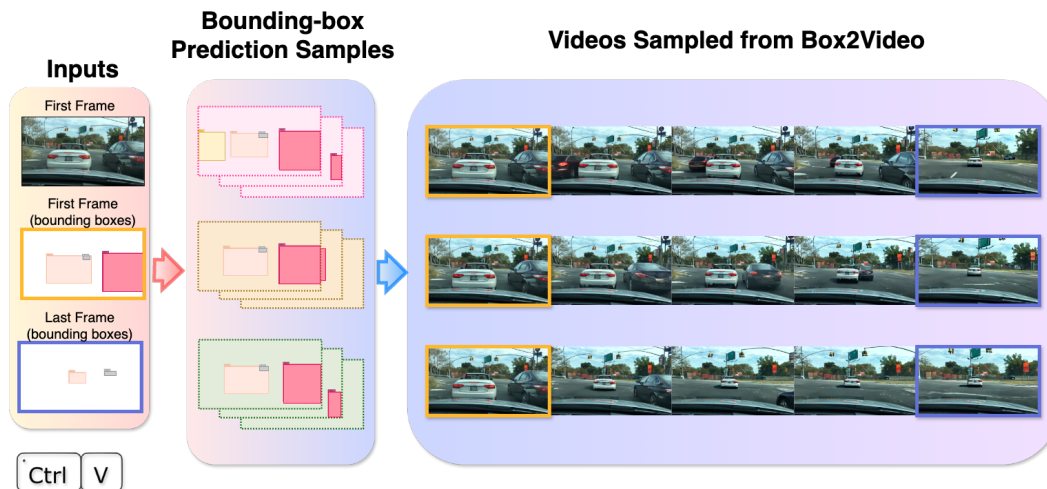


Figure 1: Overview of Ctrl-V’s generation pipeline: *Inputs (left)*: Our inputs include an initial frame, its corresponding bounding boxes and the final frame’s bounding boxes. *Bounding-box prediction samples (middle)*: We illustrate three different sequences generated from our diffusion based bounding box motion prediction model. *Videos sampled from our Box2Videodiffusion model (right)*: Our Box2Video model conditions on the predicted bounding-box samples to produce final video clips.

# 1 Introduction

There has been rapid recent progress in controllable image generation with text-to-image diffusion models [1, 2]. Given conditioning such as sketches, depth maps, segmentation maps, skeleton poses, etc. one can now generate highly realistic images adhering to the given conditioning. However, to more accurately model the real world for applications like autonomous vehicle navigation and safety one needs to account for time.

It is widely recognized that most of the state-of-the-art, real-world autonomous vehicles systems are trained and/or tested in some manner in simulation. Current AV simulators generally rely on traditional hand-engineered computer graphics environments, as exemplified by the well-known (open source) CARLA simulator [3]. However, multiple experts in the field have envisioned a future where it is possible to construct simulators from generative models, potentially revolutionizing the way we train and test autonomous vehicles. Commercial grade neural sensor simulation approaches, like the one described by Yang et al., are starting to emerge publicly.

In this work, we focus upon the specific task of generating higher fidelity controllable video through developing a method that generates first person vehicle videos conditioned on predictions of 2D and 3D bounding boxes. Our method uses a diffusion approach to predict the motions and dynamics of objects in the form of sequences of bounding boxes, and generates video according to those bounding boxes. In our experiments, we verify that it is possible to generate video that adheres tightly to the desired bounding box motion conditioning, accurately depicting desired object movements. Additionally, it allows for supervisions on the appearance and disappearance of objects in a scene, including cars, pedestrians, bikers, and others. We call our approach **Ctrl-V**, a diffusion based bounding-box conditional video generation method that makes the following contributions and addresses multiple challenges associated with generating higher fidelity video from diffusion techniques:

1. **2D-Bounding-Box and 3D-Bounding-Box Conditioning:** Unlike our prior work, our approach extends beyond merely managing motion with 2D-bounding boxes; it also permits 3D-bounding boxes to control image generation, providing an even more detailed level of control.
2. **Bounding-box Motion Predictions with Diffusion:** We present a novel diffusion based approach for predicting bounding-box *trajectories* based on their initial and final states.
3. **Uninitialized Object Generation:** Most bounding-box based generation only concerns with objects that are either present throughout the entire clip, or objects that are present at least in the first frame and persist for a while until the middle of the clip. New bounding boxes that appear after the first frame are often discarded or not accounted for [5]. In this work, we train our model to be sensitive to all bounding boxes whether they are present from the first frame and on, or only appear from the middle of the clip.
4. **A New Benchmark for a New Problem Formulation:** Given the novelty of our problem formulation, there is no existing standard way to evaluate models that seek to predict vehicle video with high fidelity. We therefore present a new benchmark consisting of a particular way of evaluating video generation models using the KITTI [6], Virtual KITTI 2 (vKITTI) [7] and the Berkeley Driving Dataset (BDD 100k) [8].

# 2 Related Work

**Video latent diffusion models (VLDMs)** extend latent image diffusion techniques [9] to video generation. Early VLDMs [10, 11, 12, 13, 14] shows temporally consistent frame generation and are tailored for text-prompted or image-prompted video generation. However, these models often struggle with complex scenes and lack the capability for precise local control.

**Conditional Video Diffusion** techniques providing a certain degree of control. Methods like VideoCompose [15], Dreamix [16], Pix2Video [17], and DreamPose [18] propose various designs of novel adapters on top of VLDMs in order to incorporate different conditioning to achieve frame-level control. **ControlNet Adapted Video Diffusion**, on the other hand, achieve precise regional or pixel-

level control in video generation by utilizing ControlNet [1] adapters within VLDM frameworks. Models such as Control-A-Video [19], Video ControlNet [20, 21], ControlVideo [22], and ReVideo [23] show that these adapters are highly adaptable to various types of conditioning, easy to train, and allow for more precise manipulation and enhanced accuracy in editing and creating video content.

**Motion Control with Bounding-Box Conditioning** There are many strategies of control that have been explored in controllable video generation research. Notably, ControlVideo [22] utilizes a training-free strategy that employs pre-trained image LDMs and ControlNets to generate videos based on *canny edge and depth maps*. Control-A-Video [19] leverages a controllable video LDM that combines a pre-trained text-to-video model with ControlNet to manipulate videos using *similar visual information*. Video ControlNets [20, 21] uses *optical flow* information to enhance video generation, while ReVideo [23] depends on extracted *video trajectories*. DreamPose [18] injects *pose sequence* information into the initial noise. VideoComposer [15] uses an array of *sketch, depth, mask, and motion vectors* as conditioning.

Many of these conditions, such as edge, depth, and optical flow maps, are costly to produce and lack the flexibility needed for customization. Bounding box emerge as a conditioning that are easily customizable and can be edited into different shape, size, locations and classes efficiently. To the best of our knowledge, five other research projects are currently exploring the use of bounding boxes for motion control in video generation. However, it is important to note that our work is distinct from these in several critical respects.

**TrailBlazer** [24] and **Peekaboo** [25] are different training-free approaches that employ attention map adjustments to direct the model in generating a particular object within a defined region. **FACTOR** [26] augmented the transformer-based generation model, Phenaki [27], by integrating a box control module. TrailBlazer, Peekaboo and FACTOR necessitate textual descriptions for individual boxes, thus lacking direct visual grounding.

Our task setup aligns closely with that of **Boximator**[5] and **TrackDiffusion** [28], in that we also do not require text descriptions for individual boxes, relying solely on bounding box inputs. However, our approaches diverge significantly. Boximator and TrackDiffusion enhance their models by introducing new self-attention layers to 3D U-Net blocks. These layers incorporate additional conditional information, such as box coordinates and object IDs, into the pretrained VLDM model. Their bounding-box information is processed using a Fourier embedder [29], which is then passed through multi-layer perceptron layers to encode. In contrast, our approach uses ControlNet and does not involve training additional encoding layers or utilizing Fourier embedder to handle the bounding-box information. Moreover, Boximator introduces a *self-tracking technique* to ensure adherence to bounding-box in generated outputs, a technique also adopted by TrackDiffusion. This enables the network to learn the object tracking task alongside video generation, but requires a two-stage training process: one with target bounding boxes in frames, and another with the boxes removed. They demonstrate that without this technique, the model’s performance markedly declines. Conversely, our model achieves alignment with the bounding-box conditions without additional training.

**Vehicle Oriented Generative Models** DriveDreamer [30] presents noteworthy contribution from autonomous driving domain. It takes an action-based approach to video simulation. It also makes use of bounding boxes and generate actions along with a video rendering. Within the DriveDreamer framework, Fourier embeddings [29] are also employed to encode bounding-box information, and CLIP embeddings [31] are used for box categorization. They focus on generating multiple camera views and do not condition on bounding box sequences, so cannot be directly compared with our problem setting. In contrast, the DriveGAN work of [32] aims to learn a GAN based driving environment in pixel-space, complete with actions and an implicit model of dynamics encoded using the latent space of a VAE. While driving oriented, the approach does not focus on controlling the generation of vehicle video that respects well-defined object trajectories with high fidelity.

### 3 Our Method: Ctrl-V

In this section, we outline our simple yet robust method for creating video clips that strictly adhere to specified frame-level bounding-box guidelines. Our approach has two steps, involving the training

of two distinct models: 1) the fine-tuning of a Video Latent Diffusion Model (VLDM) to predict bounding-box frames (Section 3.3) – which are images of only bounding boxes; 2) the training of our Box2Video to enable precise frame-level conditioning (Section 3.4).

### 3.1 Preliminaries

Stable Video Diffusion (SVD) [10, 11] is a cutting-edge video generation model that excels in converting still images into dynamic video sequences. The pretrained SVD model employed in this project has been pretrained using the Euler discrete noise scheduling method outlined by Karras et al. [33]. The objective of the SVD model is to generate a video sequence  $\mathbf{f} = [\mathbf{f}^{(0)}, \dots, \mathbf{f}^{(N)}]$  starting from an initial frame  $\mathbf{f}^{(0)}$ , where  $N$  represents the sequence length.

The SVD model utilizes an image autoencoder to encode and decode each frame, converting them between pixel space and latent space. Mathematically, this process is represented as  $\mathcal{D}(\mathcal{E}(\mathbf{f})) = \mathcal{D}(\mathbf{z}) \approx \mathbf{f}$ . In SVD, the diffusion process occurs within the latent space. This process entails gradually introducing noise to the latent representations. Subsequently, the denoiser network is responsible for removing this added noise from the noisy latent representations. The denoiser network, trained under the Euler discrete noise scheduling schema, can be described by the formulation:

$$\mathbb{D}_\theta(\mathbf{z}; \sigma_t) = \lambda_{\text{skip}}(\sigma_t)\mathbf{z} + \lambda_{\text{out}}(\sigma_t)\mathbb{U}_\theta(\lambda_{\text{in}}(\sigma_t)\mathbf{z}, \mathbf{z}_{\text{pad}}^{(0)}, \mathbf{c}^{(0)}; \lambda_{\text{noise}}(\sigma_t)) \quad (1)$$

Here  $\lambda_{\text{skip}}$ ,  $\lambda_{\text{out}}$  and  $\lambda_{\text{in}}$  are scaling functions, the mathematical definitions of which can be found in the work of Karras et al. [33].  $\mathbb{U}_\theta$  represents the 3D U-Net [34], whose parameters  $\theta$  are optimized for the denoising task during training.

To gain a clearer understanding of the U-Net inputs, we eliminate the scaling terms and reparameterize its input as follows:

$$\mathbb{U}_\theta(\hat{\mathbf{z}}_t, \mathbf{z}_{\text{pad}}^{(0)}, \mathbf{c}^{(0)}, t) \quad (2)$$

where  $\hat{\mathbf{z}}_t \in \mathbb{R}^{N, C', H', W'}$  denotes the latent representation of frames corrupted by noise at the current noise level  $t$ ;  $\mathbf{z}^{(0)} \in \mathbb{R}^{1, C', H', W'}$  represents the latent representation of the initial frame, and  $\mathbf{c}^{(0)}$  represents the encoding of the initial frame image token using CLIP [31]. These parameters are introduced into the U-Net through distinct layers. Initially, at the input layer,  $\mathbf{z}^{(0)}$  undergoes repeated padding along the frame’s time dimension to match the dimensions of the  $\hat{\mathbf{z}}_t$  tensor, namely  $\mathbf{z}_{\text{pad}}^{(0)}$ . Subsequently, the  $\mathbf{z}_{\text{pad}}^{(0)}$  is concatenated with  $\hat{\mathbf{z}}_t$  along the channel dimension and passed into the network’s input layer. Meanwhile, the noise level indicator  $t$  is transformed into a time-step embedding vector and is subsequently fed into each U-Net block along with  $\mathbf{c}^{(0)}$  via cross-attention conditioning mechanism [9].

### 3.2 Preprocessing: Bounding-Box Frame Preparation

Instead of resorting to Fourier transform or other sequential models to encode bounding-box information in string format, we have chosen to represent the bounding boxes through image rendering. We created a method to make bounding-box plots which have significant benefits. These plots not only show the precise locations of objects within a scene but also effectively display different kinds of information, like track IDs and object types, using different shapes and colors. We also implement a method to render trajectory frames, similar to the bounding-box frames, but without the pixel-space size information of the objects. These trajectory frames only contain mid-point location information. The procedure for creating bounding-box/trajectory plots is detailed in Appendix A.1. Additionally, we utilize the image-encoder ( $\mathcal{E}$ ) to encode the bounding-box frames, and its performance is discussed in Appendix A.2.

### 3.3 Ctrl-V: BBox Predictor

Our bounding-box predictor aims to forecast object positions across intermediate frames, utilizing the initial frame, initial bounding-box frame(s) and the final bounding-box/trajectory frame as references. Our approach involves adjusting the SVD network and leveraging it to generate bounding-box

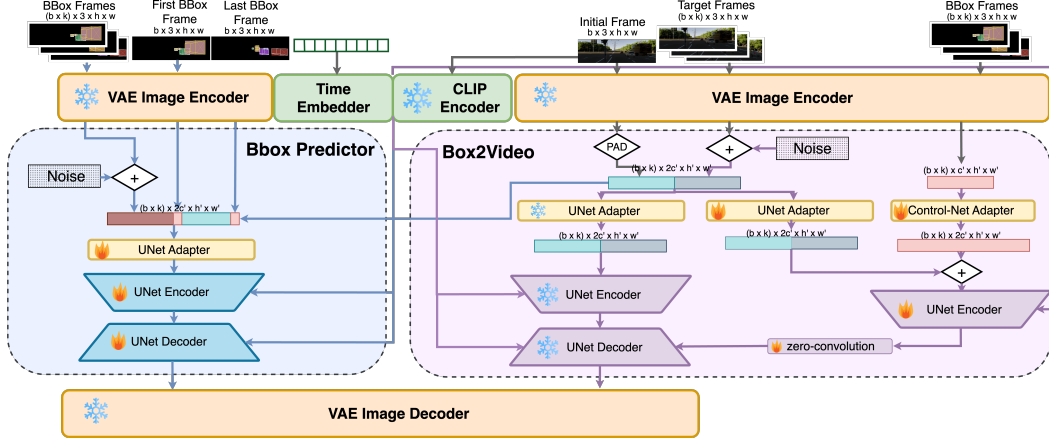


Figure 2: The overview of Ctrl-V: (left) BBox Predictor and (right) Box2Video.

frames. Specifically, we modify the inputs of the U-Net, namely  $z_t$ ,  $z_{\text{pad}}^{(0)}$ , and  $c^{(0)}$  (refer to Equation 2), to achieve this objective.

Initially, we pass the bounding-box frames through the image encoder ( $\mathcal{E}$ ) to obtain their latent representations, denoted as  $\mathcal{E}(f_{\text{bbox}}) = \mathbf{b} \in \mathbb{R}^{N, C', H', W'}$ . Furthermore, we feed the initial frame into both the image encoder and the CLIP encoder, resulting in  $z^{(0)} \in \mathbb{R}^{1 \times C' \times H' \times W'}$  and  $c^{(0)}$  respectively.

In alignment with the original SVD configuration, we replicate the padding procedure from  $z^{(0)} \in \mathbb{R}^{1 \times C' \times H' \times W'}$  to  $z_{\text{pad}}^{(0)} \in \mathbb{R}^{N \times C' \times H' \times W'}$ . However, in this scenario, we replace the first and last entries of  $z_{\text{pad}}^{(0)}$  with  $\mathbf{b}^{(0)}$  and  $\mathbf{b}^{(N-1)}$  respectively. Moreover, depending on the desired number of initial bounding-box frame(s) for conditioning, we also experiment with substituting various numbers of the  $z^{(0)}$  frames with bounding-box frames. In Equation 3.3,  $\tilde{\mathbf{b}}$  denotes the modified tensor.

Furthermore, we replaced the  $\hat{z}_t$  in Equation 2 with  $\hat{\mathbf{b}}_t$ , where noise at level  $t$  is incorporated into  $\mathbf{b}$ . The primary objective of the denoiser network is to estimate the amount of noise introduced to  $\mathbf{b}$ .

Overall, the input to the bounding-box predictor’s U-Net is represented as  $\mathbb{U}_{\omega}^{\text{bbox}}(\hat{\mathbf{b}}_t, \tilde{\mathbf{b}}, c^{(0)}, t)$ .

### 3.4 Ctrl-V: Box2Video

Given an initial frame and its corresponding sequence of bounding boxes, our aim is to produce a video clip in which the object positions align with the bounding-box sequence. To achieve this, we introduced Box2Video network, where we adapt ControlNet for the SVD framework. Unlike previous works such as Boximator and TrackDiffusion[5, 35], this motion-control model is trained in a single-stage without requiring additional optimization criteria.

Our Box2Video comprises two main components: an SVD and a ControlNet. The input to the SVD model remains consistent with Equation 2. Regarding the ControlNet, we utilize the image encoder to encode the bounding-box frames  $\mathcal{E}(f_{\text{bbox}}) = \mathbf{b} \in \mathbb{R}^{N, C', H', W'}$ . Additionally, we incorporate an adapter layer to preprocess the bounding-box latents before adding them to the frame latents. The inputs to the ControlNet are  $\mathcal{C}_{\xi}(\mathbf{b}, \hat{z}_t, z_{\text{pad}}^{(0)}, c^{(0)}, t)$ .

The architecture of ControlNet closely resembles the contraction and mid-blocks of the SVD’s U-Net architecture, a concept introduced by [1]. Additionally, at the start of the training phase, ControlNet’s weights are initialized to match those of their mirrored layers. Similar to U-Net, the CLIP encoded token of the initial frame ( $c^{(0)}$ ) and the time-step embedding are also injected into every block within the ControlNet. Finally, the output from each ControlNet block is added to the residual path within the SVD model after zero-convolution computation.

During training, the weights of the SVD model ( $\theta$ ) are frozen, while only the weights in the ControlNet ( $\xi$ ) are updated.

## 4 Experimental Analysis and Ablation Studies

All experiments are trained on the training sets and evaluated on the testing sets. To evaluate the quality of the generated videos, we randomly select 200 frames from the testing set of each dataset as the initial frames and generated videos based on them. For each dataset, the results presented in this section are based on analyses of the 200 generations.

Furthermore, each bounding-box predictor discussed in the following section requires conditioning on ONE initial frame, ONE or THREE initial bounding-box frames and ONE final bounding-box/trajectory frame.

### 4.1 Datasets

We evaluate the performance of our models across three autonomous-vehicle datasets: KITTI [6], Virtual KITTI 2 (vKITTI) [7], and the Berkeley Driving Dataset (BDD) [8] with Multi-object Tracking labels (MOT2020).

KITTI comprises 22 real-world driving clips with 3D object labelling. vKITTI consists of 5 virtual simulated driving scenes, each offering 6 weather variants, all including 3D object labelling. BDD is a large-scale real-world driving dataset, featuring 1603 2D-labeled sequences of driving clips. Further details on dataset configurations are provided in Appendix A.3.

### 4.2 Generation Quality

	Pipeline	# Cond. BBox	FVD↓	LPIPS↓	SSIM↑	PSNR↑
KITTI	Stable Video Diffusion Baseline [11]	None	552.7	0.3504	0.4030	13.01
	BBox Predictor + Box2Video	1-to-1	467.7	0.3416	0.3241	13.21
	BBox Predictor + Box2Video	3-to-1	422.2	0.2981	0.4277	13.85
	Teacher-forced Box2Video	All	435.6	0.2963	0.4394	14.10
vKITTI	Stable Video Diffusion Baseline [11]	None	331.0	0.2852	0.5540	16.60
	BBox Predictor + Box2Video	1-to-1	400.2	0.3179	0.4714	15.78
	BBox Predictor + Box2Video	3-to-1	341.4	0.2645	0.5841	17.60
	Teacher-forced Box2Video	All	313.3	0.2372	0.6203	18.41
BDD	Stable Video Diffusion Baseline [11]	None	409.0	0.3454	0.5379	16.99
	BBox Predictor + Box2Video	1-to-1	412.8	0.2967	0.5470	17.52
	BBox Predictor + Box2Video	3-to-1	373.1	0.3071	0.5407	17.37
	BBox Predictor <sup>Traj</sup> + Box2Video	3-to-1 <sup>Traj</sup>	375.8	0.2973	0.5481	17.55
	Teacher-forced Box2Video	All	348.9	0.2926	0.5836	18.39

Table 1: Generated videos consist of 25 frames at a resolution of  $312 \times 520$ , while reported metrics from this table are evaluated at a resolution of  $256 \times 410$ . The “# Cond. BBox” column reports the number of ground-truth input bounding-box frames used by the generation pipelines. “None” indicates that no ground-truth frames are used, while “All” indicates that all ground-truth bounding-box frames are utilized. If “# Cond. BBox” is  $n$ -to- $m$ , then it represents the number of initial bounding-box frames used by the pipeline is  $n$  and the number of final bounding-box frames used by the pipeline is  $m$ . If the reported number of bounding-box frames has a superscript “Traj”, it indicates that those bounding-box frames have been replaced by trajectory frames.

To assess the quality of video generation, we compare videos generated through 3 distinct pipelines: *fine-tuned SVD baselines* (from initial frame to video), *teacher-forced Box2Video generation* (from initial frame+all bounding-box frames to video), and *bounding-box prediction with Box2Video* (from initial frame+initial bounding-box frames to video).

We evaluate our generation across four metrics: Fréchet Video Distance (FVD) [36], Learned Perceptual Image Patch Similarity (LPIPS) [37], Structural Similarity Index Measure (SSIM) [38] and Peak Signal-to-Noise Ratio (PSNR). These metrics either measure the consistency of frame pixels with the ground truth or the consistency of the frame latents extracted by another network. FVD is an exception; it evaluates the generation distribution against the ground truth’s distribution. It is important to note that while many papers report their best-out-of-K results on these metrics, due to computational constraints, we evaluate our model on a single sample for each input.

The evaluated results are reported in Table 1 and visualizations are available in Appendix C.1. These results indicate that the generation quality improves as we condition on more ground-truth bounding-box frames. Details regarding the metrics and their limitations are discussed in Appendix B.1.

### 4.3 BBox Predictor: Quantitative Evaluation

	# Cond. Frames	maskIoU $\uparrow$	maskP $\uparrow$	maskR $\uparrow$	maskIoU $\uparrow$ (first+last)	maskP $\uparrow$ (first+last)	maskR $\uparrow$ (first+last)
KITTI	1-to-1	.629 $\pm$ .212	.763 $\pm$ .188	.758 $\pm$ .176	.986 $\pm$ .012	.994 $\pm$ .008	.992 $\pm$ .009
	3-to-1	.795 $\pm$ .112	.884 $\pm$ .078	.881 $\pm$ .082	.986 $\pm$ .010	.992 $\pm$ .007	.994 $\pm$ .005
vKITTI	1-to-1	.710 $\pm$ .205	.809 $\pm$ .171	.828 $\pm$ .178	.943 $\pm$ .048	.946 $\pm$ .046	.997 $\pm$ .006
	3-to-1	.767 $\pm$ .131	.853 $\pm$ .078	.881 $\pm$ .126	.944 $\pm$ .039	.948 $\pm$ .036	.996 $\pm$ .006
BDD	1-to-1	.587 $\pm$ .214	.712 $\pm$ .194	.747 $\pm$ .187	.954 $\pm$ .047	.955 $\pm$ .047	.999 $\pm$ .002
	3-to-1 <sup>Traj</sup>	.606 $\pm$ .201	.773 $\pm$ .162	.722 $\pm$ .189	.798 $\pm$ .155	.886 $\pm$ .137	.894 $\pm$ .118
	3-to-1	.647 $\pm$ .176	.783 $\pm$ .156	.784 $\pm$ .150	.955 $\pm$ .043	.955 $\pm$ .042	.997 $\pm$ .001

Table 2: All experiments reported in this table are conditioned on 3 initial bounding-box frames and 1 final bounding-box or trajectory frame. The first three columns show evaluations on the entire generated bounding-box sequence, measuring the alignment scores between our generated bounding box predictions and ground-truth labels. The last three columns focus on testing the auto-encoding capability of the network, evaluating only the first and last frames of the generated sequence. If a dataset’s name is labelled with “Traj” superscript, it indicates that in the experiment reported in that row, the last bounding-box frame is replaced with its trajectory frame.

To evaluate the quality of our bounding-box predictions, we create mask images for both the ground-truth and predicted bounding-box sequences. The mask images are generated by converting the bounding-box frames into binary masks (details can be found in Appendix B.2). We then calculate the generated averaged mask Intersection over Union (maskIoU) scores, averaged mask Precision (maskP) scores, and averaged mask Recall (maskR) scores against the ground-truth bounding-box masks. To assess our predictions, we applied the “best-out-of-K” method, selecting the model with the highest maskIoU score for evaluation. In this instance, K equals 5. We present our findings in Table 2, and demonstrate examples of our bounding-box predictions on each dataset in Appendix C.

In the bounding-box prediction figures, our predictor model achieves the closest alignment with the ground-truth in the first and last frames. This near-perfect alignment is primarily attributed to conditioning the model on the bounding boxes of these key frames. When considering all predicted frames, the alignment scores decrease, as shown by the plotted demonstrations and metric results in Table 2. This is because objects in frames do not move deterministically. *The role of the bounding-box predictor is to generate a plausible trajectory for moving objects from the initial bounding box frame to the last.*

Despite the disparity between the ground-truth trajectory and the predicted trajectory, our Box2Video consistently generates high-fidelity videos based on either trajectory provided. Further analysis of this aspect is provided in the subsequent sections.

### 4.4 Box2Video: Motion Control Evaluation

Our Box2Video is trained to control object motions through bounding boxes using a teacher-forcing approach. This means that only ground-truth bounding-box frames are provided during the training



Figure 3: Illustrations of the generations conditioned on ground truth 3D bounding boxes (2D for BDD) across various datasets. The 2D outlines of bounding boxes are overlaid on top.

phase. In this section, we analyze the fidelity of our Box2Video generations to the ground-truth bounding-box conditions. To assess the consistency of objects’ locations between our generated content and ground-truth, we compute the average precision of the bounding boxes in the generated frames and the ground-truth frames.

Average precision (AP) scores gauge the alignment of predicted/generated bounding boxes with the ground-truth labeling. In all related prior studies, average precision (AP) scores have been consistently reported. However, it is important to acknowledge that AP scores can vary across studies, depending on the specifics of the task setup. Boximator [5]’s motion control model predicts object locations in the scene, focusing solely on objects with consistent appearances across all frames. Their AP implementation disregards the object locations in the intermediate frames, comparing the objects’ locations only in the final frame. In contrast, TrackDiffusion [35] uses TrackAP for evaluation, employing a QDTrack model [28] to track instances in generated videos and comparing them to ground-truth labels. However, these evaluated datasets have limited instances, and TrackAP requires consistent tracking across frames, making it unsuitable for our project without modifications. Therefore, our AP score differs slightly from those in previous works.

Autonomous driving datasets often contain numerous object instances within a scene, with objects continuously entering, exiting, and interacting with each other. In line with this complexity, we have introduced our own version of the AP metric in this work. Our AP metric is designed to comprehensively compare all objects across every scene: encompassing those that newly enter, those that exist during the intermediate frames, and those that overlap with others.

First, we utilize the state-of-the-art object detection tool, YOLOv8 [39], to obtain the objects’ trackings from the generated and ground-truth scenes. Detailed information about the tool and our configurations is reported in Appendix B.3. Next, we match objects in each generated-vs-ground-truth frame pair based on *spatial similarity* – calculating the intersection over union (IoU) score to determine the similarity in location between objects’ bounding boxes. Our metric disregards object type and tracking IDs equivalence – assuming that objects close in location should naturally have the same type and IDs. Finally, we compute the average precision score following MS COCO protocol [40]. Details are provided in Appendix B.4 and results are listed in Table 3. These results indicate that our Box2Video model is particularly adept at adhering to the specified conditions, especially when evaluated with a more lenient metric (i.e., a lower IoU threshold for the AP computation).

## 5 Conclusions

We present **Ctrl-V**, a novel model capable of generating controllable autonomous vehicle videos. Our approach demonstrates that the BBox Predictor model can closely follow generation requirements for the first and last frames and produce a coherent bounding-box track for the intermediate frames. We also show that our Box2Video network generates high fidelity videos, strictly adhering to the given bounding boxes. Furthermore, our model accommodates both 2D and 3D bounding

Method	Dataset	Dataset Type	# Frames	mAP $\uparrow$	AP $_{50}$ $\uparrow$	AP $_{75}$ $\uparrow$	AP $_{90}$ $\uparrow$
<b>Ctrl-V</b>	KITTI	Driving	25	0.547	0.712	0.601	0.327
	vKITTI	Driving-sim	25	0.599	0.776	0.667	0.356
	BDD	Driving	25	0.685	0.855	0.781	0.401
<b>Boximator [5]<sup>1</sup></b>	MSR-VTT[41]	Web videos	16	0.365	0.521	0.384	-
	ActivityNet [42]	Human-action	16	0.394	0.607	0.409	-
	UCF-101 [43]	Human-action	16	0.212	0.343	0.205	-
<b>TrackDiffusion[35]</b>	YTFVIS [44]	YouTube videos	16	0.467	0.656	-	-
	UCF-101 [43]	Human-action	16	0.205	0.326	-	-

Table 3: Average Precision scores of our model. While prior works [5, 35] utilize varying evaluation strategies and do not report results on KITTI, vKITTI and BDD, we draw upon their reported performances on alternative datasets to provide a comparative context. Longer videos are associated with decreased quality and lower detection rates, posing an additional challenge for our model.

boxes and handles uninitialized objects appearing in the middle of the videos. Ctrl-V provides future researchers with an efficient way to simulate driving video data with flexible controllability in the form of bounding boxes. In addition, we further define an improved metric to evaluate bounding box conditioned video generation to account for objects that are not present in the first frame, and those that do not remain until the last frame. In Appendix D, we discuss potential future work for this project. With Ctrl-V and an improved metric for more accurate evaluation, we aim to establish a solid foundation for future research in controllable video generation.

### Acknowledgments

We thank CIFAR for their support under the AI chairs program, NSERC for their support under the Discovery Grants program, and Samsung for supporting this work.

### References

- [1] L. Zhang, A. Rao, and M. Agrawala. Adding conditional control to text-to-image diffusion models, 2023.
- [2] P. Cao, F. Zhou, Q. Song, and L. Yang. Controllable generation with text-to-image diffusion models: A survey. *arXiv preprint arXiv:2403.04279*, 2024.
- [3] A. Dosovitskiy, G. Ros, F. Codevilla, A. Lopez, and V. Koltun. Carla: An open urban driving simulator, 2017.
- [4] Z. Yang, Y. Chen, J. Wang, S. Manivasagam, W.-C. Ma, A. J. Yang, and R. Urtasun. Unisim: A neural closed-loop sensor simulator, 2023.
- [5] J. Wang, Y. Zhang, J. Zou, Y. Zeng, G. Wei, L. Yuan, and H. Li. Boximator: Generating rich and controllable motions for video synthesis, 2024.
- [6] A. Geiger, P. Lenz, C. Stiller, and R. Urtasun. Vision meets robotics: The kitti dataset. *International Journal of Robotics Research (IJRR)*, 2013.
- [7] Y. Cabon, N. Murray, and M. Humenberger. Virtual kitti 2, 2020.
- [8] F. Yu, H. Chen, X. Wang, W. Xian, Y. Chen, F. Liu, V. Madhavan, and T. Darrell. Bdd100k: A diverse driving dataset for heterogeneous multitask learning, 2020.
- [9] R. Rombach, A. Blattmann, D. Lorenz, P. Esser, and B. Ommer. High-resolution image synthesis with latent diffusion models, 2022.
- [10] A. Blattmann, R. Rombach, H. Ling, T. Dockhorn, S. W. Kim, S. Fidler, and K. Kreis. Align your latents: High-resolution video synthesis with latent diffusion models, 2023.

- [11] A. Blattmann, T. Dockhorn, S. Kulal, D. Mendeleevitch, M. Kilian, D. Lorenz, Y. Levi, Z. English, V. Voleti, A. Letts, V. Jampani, and R. Rombach. Stable video diffusion: Scaling latent video diffusion models to large datasets, 2023.
- [12] Y. He, T. Yang, Y. Zhang, Y. Shan, and Q. Chen. Latent video diffusion models for high-fidelity long video generation, 2023.
- [13] Y. Zeng, G. Wei, J. Zheng, J. Zou, Y. Wei, Y. Zhang, and H. Li. Make pixels dance: High-dynamic video generation, 2023.
- [14] J. Z. Wu, Y. Ge, X. Wang, W. Lei, Y. Gu, Y. Shi, W. Hsu, Y. Shan, X. Qie, and M. Z. Shou. Tune-a-video: One-shot tuning of image diffusion models for text-to-video generation, 2023.
- [15] X. Wang, H. Yuan, S. Zhang, D. Chen, J. Wang, Y. Zhang, Y. Shen, D. Zhao, and J. Zhou. Videocomposer: Compositional video synthesis with motion controllability, 2023.
- [16] E. Molad, E. Horwitz, D. Valevski, A. R. Acha, Y. Matias, Y. Pritch, Y. Leviathan, and Y. Hoshen. Dreamix: Video diffusion models are general video editors, 2023.
- [17] D. Ceylan, C.-H. P. Huang, and N. J. Mitra. Pix2video: Video editing using image diffusion, 2023.
- [18] J. Karras, A. Holynski, T.-C. Wang, and I. Kemelmacher-Shlizerman. Dreampose: Fashion image-to-video synthesis via stable diffusion, 2023.
- [19] W. Chen, J. Wu, P. Xie, H. Wu, J. Li, X. Xia, X. Xiao, and L. Lin. Control-a-video: Controllable text-to-video generation with diffusion models, 2023.
- [20] Z. Hu and D. Xu. Videocontrolnet: A motion-guided video-to-video translation framework by using diffusion model with controlnet, 2023.
- [21] E. Chu, S.-Y. Lin, and J.-C. Chen. Video controlnet: Towards temporally consistent synthetic-to-real video translation using conditional image diffusion models, 2023.
- [22] Y. Zhang, Y. Wei, D. Jiang, X. Zhang, W. Zuo, and Q. Tian. Controlvideo: Training-free controllable text-to-video generation, 2023.
- [23] C. Mou, M. Cao, X. Wang, Z. Zhang, Y. Shan, and J. Zhang. Revideo: Remake a video with motion and content control, 2024.
- [24] W.-D. K. Ma, J. P. Lewis, and W. B. Kleijn. Trailblazer: Trajectory control for diffusion-based video generation, 2024.
- [25] Y. Jain, A. Nasery, V. Vineet, and H. Behl. Peekaboo: Interactive video generation via masked-diffusion, 2024.
- [26] H.-P. Huang, Y.-C. Su, D. Sun, L. Jiang, X. Jia, Y. Zhu, and M.-H. Yang. Fine-grained controllable video generation via object appearance and context, 2023.
- [27] R. Villegas, M. Babaeizadeh, P.-J. Kindermans, H. Moraldo, H. Zhang, M. T. Saffar, S. Castro, J. Kunze, and D. Erhan. Phenaki: Variable length video generation from open domain textual description, 2022.
- [28] T. Fischer, T. E. Huang, J. Pang, L. Qiu, H. Chen, T. Darrell, and F. Yu. Qdtrack: Quasi-dense similarity learning for appearance-only multiple object tracking, 2023.
- [29] B. Mildenhall, P. P. Srinivasan, M. Tancik, J. T. Barron, R. Ramamoorthi, and R. Ng. Nerf: Representing scenes as neural radiance fields for view synthesis, 2020.
- [30] X. Wang, Z. Zhu, G. Huang, X. Chen, J. Zhu, and J. Lu. Drivedreamer: Towards real-world-driven world models for autonomous driving, 2023.

- [31] A. Radford, J. W. Kim, C. Hallacy, A. Ramesh, G. Goh, S. Agarwal, G. Sastry, A. Askell, P. Mishkin, J. Clark, G. Krueger, and I. Sutskever. Learning transferable visual models from natural language supervision. *CoRR*, abs/2103.00020, 2021. URL <https://arxiv.org/abs/2103.00020>.
- [32] S. W. Kim, J. Phillion, A. Torralba, and S. Fidler. Drivegan: Towards a controllable high-quality neural simulation, 2021.
- [33] T. Karras, M. Aittala, T. Aila, and S. Laine. Elucidating the design space of diffusion-based generative models, 2022.
- [34] O. Ronneberger, P. Fischer, and T. Brox. U-net: Convolutional networks for biomedical image segmentation, 2015.
- [35] P. Li, K. Chen, Z. Liu, R. Gao, L. Hong, G. Zhou, H. Yao, D.-Y. Yeung, H. Lu, and X. Jia. Trackdiffusion: Tracklet-conditioned video generation via diffusion models, 2024.
- [36] T. Unterthiner, S. van Steenkiste, K. Kurach, R. Marinier, M. Michalski, and S. Gelly. Towards accurate generative models of video: A new metric & challenges, 2019.
- [37] R. Zhang, P. Isola, A. A. Efros, E. Shechtman, and O. Wang. The unreasonable effectiveness of deep features as a perceptual metric, 2018.
- [38] Z. Wang, A. Bovik, H. Sheikh, and E. Simoncelli. Image quality assessment: from error visibility to structural similarity. *IEEE Transactions on Image Processing*, 13(4):600–612, 2004. doi:10.1109/TIP.2003.819861.
- [39] D. Reis, J. Kupec, J. Hong, and A. Daoudi. Real-time flying object detection with yolov8, 2024.
- [40] T.-Y. Lin, M. Maire, S. Belongie, L. Bourdev, R. Girshick, J. Hays, P. Perona, D. Ramanan, C. L. Zitnick, and P. Dollár. Microsoft coco: Common objects in context, 2015.
- [41] J. Xu, T. Mei, T. Yao, and Y. Rui. Msr-vtt: A large video description dataset for bridging video and language. In *2016 IEEE Conference on Computer Vision and Pattern Recognition (CVPR)*, pages 5288–5296, 2016. doi:10.1109/CVPR.2016.571.
- [42] F. C. Heilbron, V. Escorcia, B. Ghanem, and J. C. Niebles. Activitynet: A large-scale video benchmark for human activity understanding. In *2015 IEEE Conference on Computer Vision and Pattern Recognition (CVPR)*, pages 961–970, 2015. doi:10.1109/CVPR.2015.7298698.
- [43] K. Soomro, A. R. Zamir, and M. Shah. UCF101: A dataset of 101 human actions classes from videos in the wild. *CoRR*, abs/1212.0402, 2012. URL <http://arxiv.org/abs/1212.0402>.
- [44] L. Yang, Y. Fan, and N. Xu. Video instance segmentation. *CoRR*, abs/1905.04804, 2019. URL <https://arxiv.org/abs/1905.04804>.
- [45] P. von Platen, S. Patil, A. Lozhkov, P. Cuenca, N. Lambert, K. Rasul, M. Davaadorj, D. Nair, S. Paul, W. Berman, Y. Xu, S. Liu, and T. Wolf. Diffusers: State-of-the-art diffusion models. <https://github.com/huggingface/diffusers>, 2022.
- [46] I. Loshchilov and F. Hutter. Decoupled weight decay regularization, 2019.
- [47] Z. Wang and A. C. Bovik. Mean squared error: Love it or leave it? a new look at signal fidelity measures. *IEEE Signal Processing Magazine*, 26(1):98–117, 2009. doi:10.1109/MSP.2008.930649.
- [48] Z. Wang, A. Bovik, H. Sheikh, and E. Simoncelli. Image quality assessment: from error visibility to structural similarity. *IEEE Transactions on Image Processing*, 13(4):600–612, 2004. doi:10.1109/TIP.2003.819861.

- [49] Z. Kotevski and P. Mitrevski. Experimental comparison of psnr and ssim metrics for video quality estimation, 01 2010.
- [50] M. Sharif, L. Bauer, and M. K. Reiter. On the suitability of  $l_p$ -norms for creating and preventing adversarial examples. *CoRR*, abs/1802.09653, 2018. URL <http://arxiv.org/abs/1802.09653>.
- [51] G. Jocher, A. Chaurasia, and J. Qiu. Ultralytics YOLO, Jan. 2023. URL <https://github.com/ultralytics/ultralytics>.
- [52] N. Aharon, R. Orfaig, and B.-Z. Bobrovsky. Bot-sort: Robust associations multi-pedestrian tracking. *arXiv preprint arXiv:2206.14651*, 2022.

## A Implementation Details

### A.1 Step-by-Step Guide to Plotting Bounding Box Frames

We create bounding-box plots for each frame according to the following steps:

1. Each unique track ID is randomly assigned a specific color, and the random color selected has values exceeding 50 across all RGB channels.
2. Each unique object class label is assigned a distinct color.
3. For each object, we fill the 2D bounding-box region with its track ID’s color at 75% transparency. This transparency allows the overlapping regions of the boxes to remain visible.
4. If 3D bounding-box information is available for an object, we draw the 3D bounding boxes and outline them with the color corresponding to the object’s class label.
5. If 3D bounding-box information is unavailable, we outline the 2D bounding-box with the color corresponding to the object’s class label. Moreover, we mark an X at the rear face of each 3D bounding-box for enhanced contextualization.
6. In certain experiments, we substitute bounding-box plots with trajectory plots. To create a trajectory plot, we first compute the mid-points of its 2D bounding boxes. Subsequently, at each bounding-box midpoint, we draw a circle with a diameter of 10 pixels, filled with the color corresponding to its track ID. Within this circle, we draw a smaller circle with a diameter of 5 pixels, filled with the color representing the object’s class label.

### A.2 Bounding-Box Visualization and Reconstruction Analysis

In this work, we refrain from introducing new modules dedicated to encoding the bounding-box frames. Instead, we leverage the encoder ( $\mathcal{E}$ ) within the SVD’s autoencoder framework. Our experiments demonstrate the efficacy of the SVD autoencoder in accurately encoding and decoding bounding-box frames.

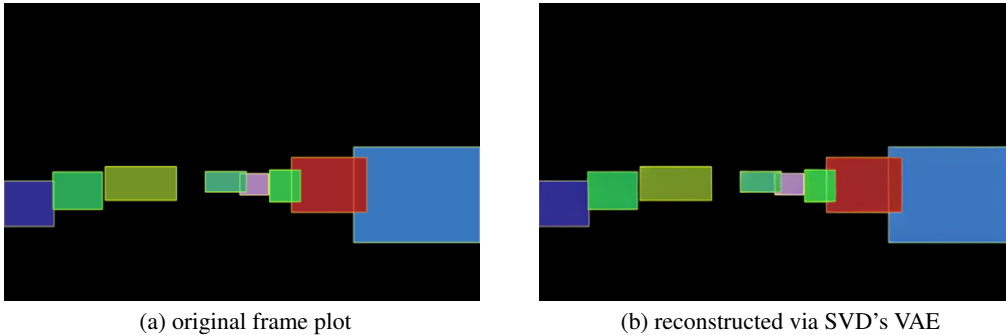


Figure 4: Visualizing a BDD100K 2D-bbox frame created using the method described in A.1

### A.3 Dataset Configuration

**KITTI:** The downloadable content of the official KITTI dataset does not include bounding-box label files for the testing set. As a result, we manually partition the dataset’s training folder into two segments for our experiments. The training split encompasses samples ‘0000’ to ‘0018’, while the testing split consists of samples ‘0019’ and ‘0020’.

**Virtual-KITTI 2 (vKITTI):** We’ve not found specification of the train/test split on the official website. During training, we exclude ‘Scene20’, and the models were trained on the remaining four scenes.

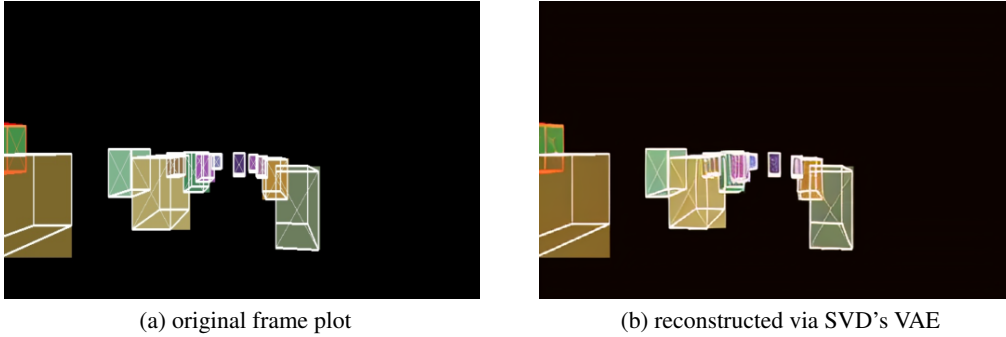


Figure 5: Visualizing a VKITTI 3D-bbox frame created using the method described in A.1

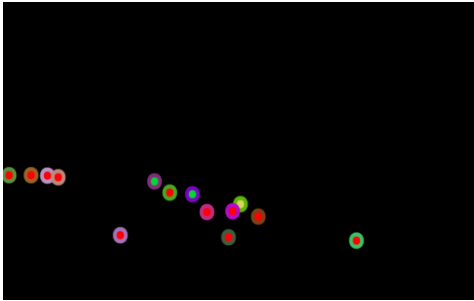


Figure 6: Visualizing a BDD100K trajectory frame created using the method described in A.1.

**BDD100k:** We adhere to the official train/validation split for our training and testing phases.

In our experiments, we standardize the frame sizes for all experiments to  $312 \times 520$  and set a clip length of 25 frames. All experiments are trained using the training set and assessed using the validation or test sets. Unless otherwise stated, the results and the visualizations provided are derived from the test sets.

#### A.4 Training Configuration

Our pretrained SVD models are adaptations from HuggingFace’s diffuser library [45]. Specifically, we utilize the ‘stable-video-diffusion-img2vid-xt’ SVD variant in this project.

We have trained various types of bounding-box predictors in this work: 1. *3D bounding-box predictor (3-to-1)* 2. *2D bounding-box predictor (3-to-1)* 3. *2D bounding-box-trajectory predictor (3-to-1<sup>Traj</sup>)*.

The 3D bounding-box predictor anticipates frames using 3D bounding boxes, while the 2D predictor does the same for 2D bounding boxes. A 1-to-1 model predicts frames between the first and last bounding-box frames, while a 3-to-1 model predicts frames between the first 3 and last bounding-box frames. Additionally, there’s a bounding-box-trajectory model where the last conditional frame is a trajectory frame instead of a bounding-box frame.

For the bounding-box predictors trained on KITTI or vKITTI datasets, each model undergoes 5 epochs of training. The 2D bounding-box predictor (1-to-1) is trained on BDD100K for 33,000 iterations. Additionally, the 2D bounding-box (3-to-1) and 2D bounding-box-trajectory (3-to-1) models start their fine-tuning process for an additional 15,000 iterations from where the 2D bounding-box predictor (1-to-1)’s training ends. All of these prediction models are trained on a single A100 GPU with a batch size of 1. We also set gradient accumulation steps to 5 and employed AdamW [46] as our optimizer.

The fine-tuning and training procedures for the baseline Stable Diffusion and the ControlNet models are almost the same as of the bounding-box predictor model. The only difference is that we trained our baseline and ControlNet for 48,000 iterations on BDD100K.

## B Evaluation Details

### B.1 Generation Quality Metrics: PSNR, SSIM, LPIPS and FVD

**PSNR**, or Peak signal-to-noise ratio, calculates the ratio between the maximum value of a signal and the noise that affects the fidelity of its representation. It is closely related to Mean Squared Error (MSE) loss. It can be in fact calculated by subtracting the log of MSE from a constant. It is long been used as a metric for image reconstruction quality for its ease of use and mathematical properties. However, PSNR suffers multiple issues as a metric for image generation tasks. Its insensitiveness to various distortion such as blurring, pepper noise, and mean-shifting means that image pairs that look very different to human can have very similar PSNR scores [47, 48].

**SSIM**, or Structural similarity index measure, is a metric that aims to evaluate similarity in "structures" of image pairs – as opposed to absolute errors as in the cases of MSE and PSNR. Because the human visual system is more sensitive to structural distortions, this metric is more closely aligned with human evaluation compared to PSNR. However, some visually apparent distortions are not captured by the SSIM. Things like changing hue and brightness do not seem to affect SSIM much [49] and Sharif et al. [50] presents more examples of unpredictable ssim behaviours when presented with different distortions.

**LPIPS**, or Learned Perceptual Image Patch Similarity [37], is a neural network based approach to accessing image similarity. It does so by computing distance between some representation of image patches. These representations are obtained by running image patches through some pre-defined neural network. LPIPS has been shown to math human perception well.

**FVD**, or Fréchet Video Distance [36], is a metric for generative video models. It is based on the Fréchet inception distance (FID) for images. Unlike the 3 other metrics that focuses on image frames and do not consider their temporal relationships, FVD is specifically designed for videos. It takes into consideration the visual quality, temporal coherence, and diversity of samples of videos generated by the model under evaluation. The large scale human study carried out by the authors suggest FVD consistently agrees with human evaluation of videos.

### B.2 Prediction Scores: Converting Bounding-Box Frames to Binary Masks

*To convert ground-truth bounding box frames into binary masks*, we combine all color channels and assign a value of 1 to all non-black pixels.

*To transform predicted bounding-box frames into binary masks*, we first need to perform post-processing on the frames. These frames originate from a network output, and although background pixels that seem black, they may not all be precisely zero. To prevent these pixels being detected as bounding-box masks, we aggregate the pixel values across color channels, and for those channels whose sum is below 50, we convert them to black pixels. Subsequently, we convert the frames into binary masks by aggregating all channels and changing the colored pixel values to 1.

The maskIoU score measures the averaged ratio of the intersection area to the union area of the masks. The maskP score evaluates the averaged ratio of the intersection area to the predicted mask, while the maskR score quantifies the averaged ratio of the intersection area to the ground-truth mask.

Accurately evaluating bounding-box predictions remains challenging. We recognize that our current metrics (maskIoU, maskR and maskP), which rely on binary masks to evaluate the performance of bounding-box predictors, have limitations as they do not consider object tracking IDs (the colors of the bounding boxes). However, we still believe that the metric evaluations using binary masks can offer valuable insights into our model’s performance.

### B.3 Motion Control Assessment: YOLOv8 Object Detector Configurations

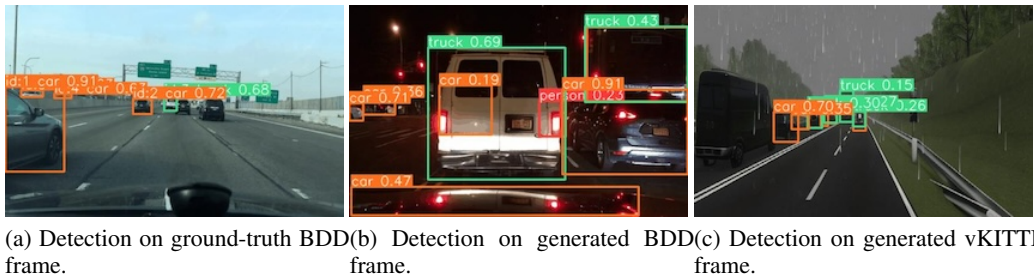


Figure 7: YOLOv8 detections on BDD and vKITTI with confidence thresholds set to 0.1. The detection confidence scores are labeled on the detected bounding boxes.

We utilize the “yolov8x” variant of the YOLOv8 model, implemented by Ultralytics [51], for object detection. We set the detector’s Non-Maximum Suppression Intersection Over Union (NMS-IoU) threshold to be 0.35 across all experiments.

Since YOLOv8 was trained to detect objects from the MS COCO dataset [40], we adjust the class labels of our dataset to match the MS COCO labels using the following mappings:

<b>KITTI</b>	CAR-CAR; VAN-CAR; TRUCK-TRUCK; PEDESTRIAN-PERSON; PERSON-PERSON; CYCLIST-PERSON; TRAM-TRAIN
<b>vKITTI</b>	CAR-CAR; VAN-CAR; TRUCK-TRUCK; TRAM-TRAIN
<b>BDD</b>	PEDESTRIAN-PERSON; RIDER-PERSON; CAR-CAR; TRUCK-TRUCK; BUS- BUS; TRAIN-TRAIN

Table 4: Mappings of various dataset labels to MS COCO labels.

The detection resolution is maintained at the same level as the generation/training resolution –  $312 \times 520$ .

YOLOv8 is a powerful tool, especially for object detection tasks. Its detection results are very impressive but not always perfect, which leaves rooms for errors when relying on its output to evaluate our model’s performance. Two examples of YOLOv8’s detection on generated and ground-truth BDD frames are illustrated in Figure 7.

In the ground-truth BDD frame detections, the network has missed detecting the two black SUVs on the right, even though the confidence threshold is set as low as 0.1 during detection.

In the generated BDD frame detections, the network has falsely detected the reflections on the engine hood of the driving vehicle as a car. This is a common mislabeling we have observed across the experiments.

In the last example, we demonstrate that YOLOv8 can generate detections on virtual datasets such as vKITTI.

We have attempted to enhance our detection results across frames by using a tracker in conjunction with the YOLOv8 detector. Specifically, we use the BoT-SORT [52] tracker. However, we’ve observed an increase in the precision but a significant drop in the recall of the detection scores. Thus, we’ve reverted to using only the YOLOv8 detection model to compute the AP metrics.

#### B.4 Motion Control Assessment: Average Precision Calculation

Average precision (AP) is the area under the recall-precision curve; it takes into account the trade-off between precision and recall at different confidence thresholds. It serves as a measure to evaluate how well the predicted or generated bounding boxes correspond to the actual ground-truth labels.

Prior to developing our custom AP metrics, we conduct experiments to assess YOLOv8’s performance on our datasets. We evaluate YOLOv8 and YOLOv8+BoT-SORT on our three datasets using detection and tracking experiments. We employ Track-mAP to evaluate the alignment score between the detections on the ground-truth frames and actual ground-truth labels. The results are not satisfactory; the detection recall is low, suggesting a significant number of missed detections. This issue was exacerbated when using BoT-SORT for tracking. These results lead us to deviate from utilizing the ground-truth labeling and instead use the detections from the ground-truth frames as the labels for our mAP calculations.

We begin by employing a YOLOv8 detection model on both the generated and ground-truth videos, yielding a series of bounding-box detections for each. When we generate bounding-box detections on ground-truth videos, we keep the confidence cutoff fixed at 0.6.

Next, we calculate the AP scores at different IoU thresholds following the MS COCO protocol [40]: compute 10 AP scores at IoU thresholds ranging from 0.5 to 0.95, in increments of 0.05. The AP score computed at threshold  $\tau$  is referred to as  $AP_{\tau \times 100}$ . Mean average precision (mAP) is the average of all the AP scores. The computed results are reported in Table 3.

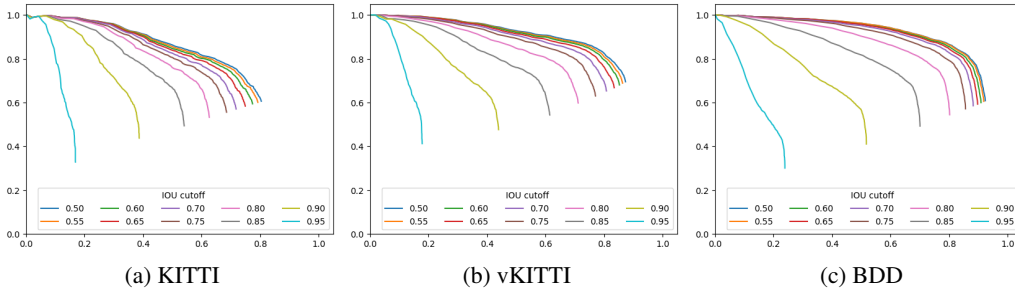


Figure 8: Precision-recall curves: the x-axis represents the recall rate, and the y-axis represents the precision rate.

Figure 8 contains the precision-recall curves of the three datasets. The precision-recall curves are computed by dividing confidence cut-off into 100 intervals ranging from 0.01 to 1.00. Each curve presents the precision-recall trade-off by adjusting the confidence cutoff while keeping the IoU cutoff constant.

Our precision-recall curves typically lie above the diagonal line, indicating that our precision is generally higher than our recall. This further implies that if the detector identifies an object in our generated frame, there is a high likelihood that an object is detected in the same location in the ground-truth frame. On the other hand, the lower recall rate implies that an object may not always be present (or detected) in the same location as identified by the detector in the ground-truth frame.

Several factors could have affected the recall rate:

- *Generation quality*: The quality of the generated images can influence the detectability of objects, thereby affecting the recall rate.
- *Detection error*: The performance of the detector has a direct impact on the recall rate. If there are many missed detections, the recall rate will also be high.
- *Data error*: This includes mislabeled samples from the dataset and our data preprocessing method. We limit the number of bounding boxes in a frame to a maximum of 15. Conse-

quently, there may be missing bounding boxes for objects in the scene, which could affect our recall rate.

On another note, an ideal precision-recall curve would be a horizontal line at  $y = 1$ . This would indicate perfect precision and recall across all thresholds. Among the 3 experiments, our precision-recall curve for BDD is closest to this ideal line. One reason for this is that the BDD dataset contains significantly more data compared to the others, which can significantly boost our generation results.

## C Generation Results

### C.1 Stable Video Diffusion vs Box2Video: Generation Quality Comparison

The following are generation comparisons between the fine-tuned Stable Video Diffusion baseline model and the Box2Video conditioned on the ground-truth bounding-box frames. All visualizations are generated using the BDD100k dataset.



(a) Stable Video Diffusion's generation at frame 13



(b) Box2Video's generation at frame 13

Figure 9: Comparison of an urban scene generation between the baseline Stable Video Diffusion (SVD) model and the teacher-forced Box2Video model.



(a) Stable Video Diffusion's generation at frame 13



(b) Box2Video's generation at frame 13

Figure 10: Comparison of a crowded intersection scene generation between the baseline Stable Video Diffusion (SVD) model and the teacher-forced Box2Video model.



(a) Stable Video Diffusion's generation at frame 13



(b) Box2Video's generation at frame 13

Figure 11: Comparison of a night scene generation between the baseline Stable Video Diffusion (SVD) model and the teacher-forced Box2Video model. Ground-truth bboxes are outlined.

## C.2 BDD Result Visualizations: Bounding-Box Predictions and Motion-Controlled Video Generations

In the following section, we showcase a range of BDD generation results produced by our 3-to-1 generation pipeline in different scene scenarios, such as city, urban, highways, busy intersections and at night. Each visualization displays every 6th frame from a 25-frame clip, with the actual video generated at a frame rate of 5 fps. In the leftmost column labels, GT represents ground truth, PB represents predicted bounding-box frames, and PF represents predicted frames.

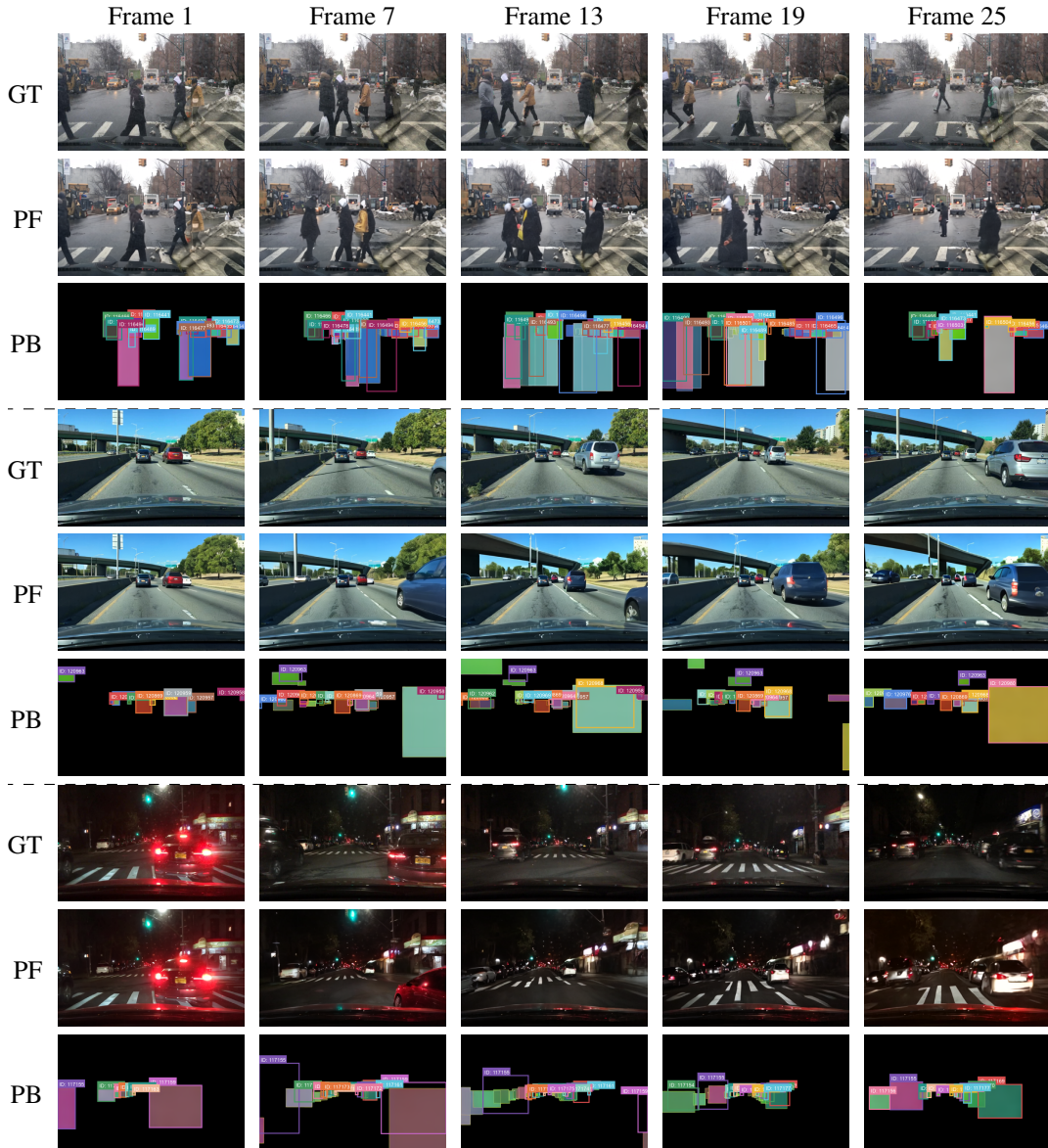


Figure 12: 2D bounding-box frame predictions and motion-controlled video generations for various scenes.



Figure 13: 2D bounding-box frame predictions and motion-controlled video generations for various scenes.

### C.3 vKITTI Result Visualizations: 3D Bounding-Box Predictions and Motion Controlled Video Generations

In the following section, we showcase a range of vKITTI generation results produced by our 3-to-1 generation pipeline in different scene scenarios. In Figure 14, we showcase our generations on the vKITTI test split. However, it is worth noting that the vKITTI test split comprises samples from only one type of scene (unseen during training). To provide a broader perspective, in Figure 15, we present additional results on the vKITTI train split. Each visualization displays every 6th frame from a 25-frame clip, with the actual video generated at a frame rate of 7 fps. In the leftmost column labels, GT represents ground truth, PB represents predicted bounding-box frames, and PF represents predicted frames.

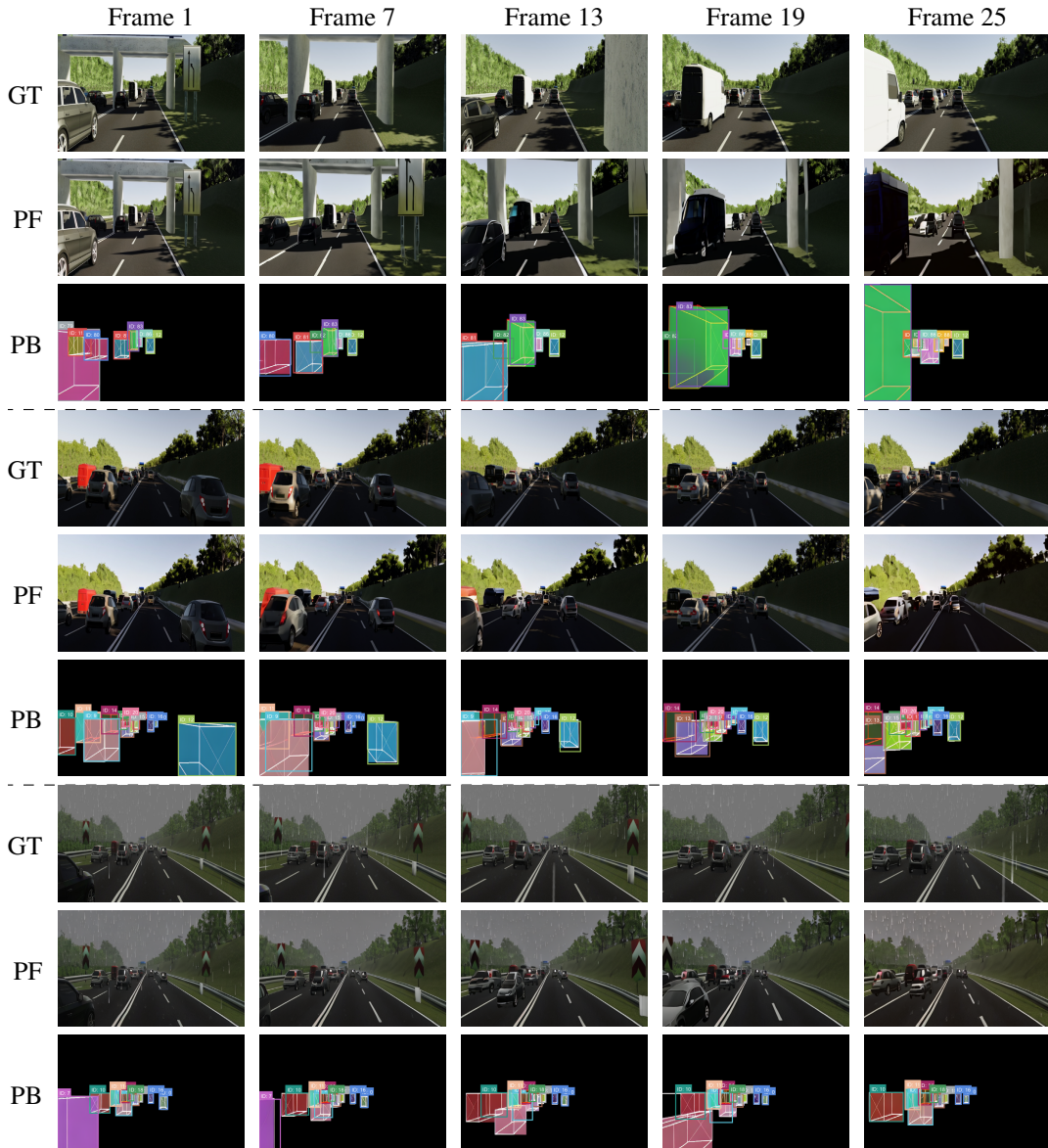


Figure 14: 3D bounding-box predictions and motion-controlled video generations for various scenes on vKITTI test-split.

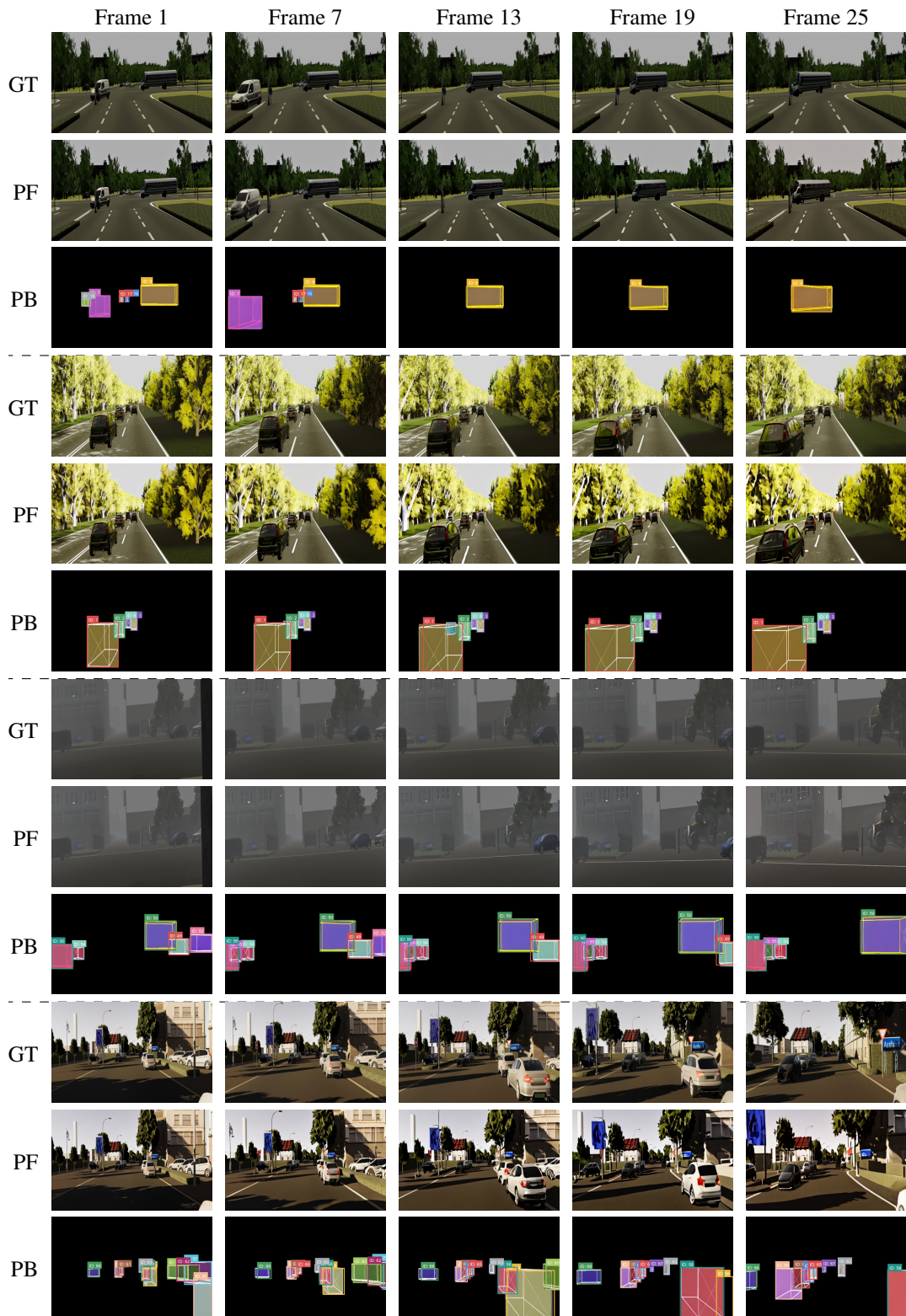


Figure 15: 3D bounding-box predictions and motion-controlled video generations for various scenes on vKITTI train-split.

#### C.4 KITTI Result Visualizations: Bounding-Box Predictions and Motion-Controlled Video Generations

In the following section, we showcase a range of KITTI generation results produced by our 3-to-1 generation pipeline in different scene scenarios, such as urban area, city streets and highway. Each visualization displays every 6th frame from a 25-frame clip, with the actual video generated at a frame rate of 7 fps. In the leftmost column labels, GT represents ground truth, PB represents predicted bounding-box frames, and PF represents predicted frames.

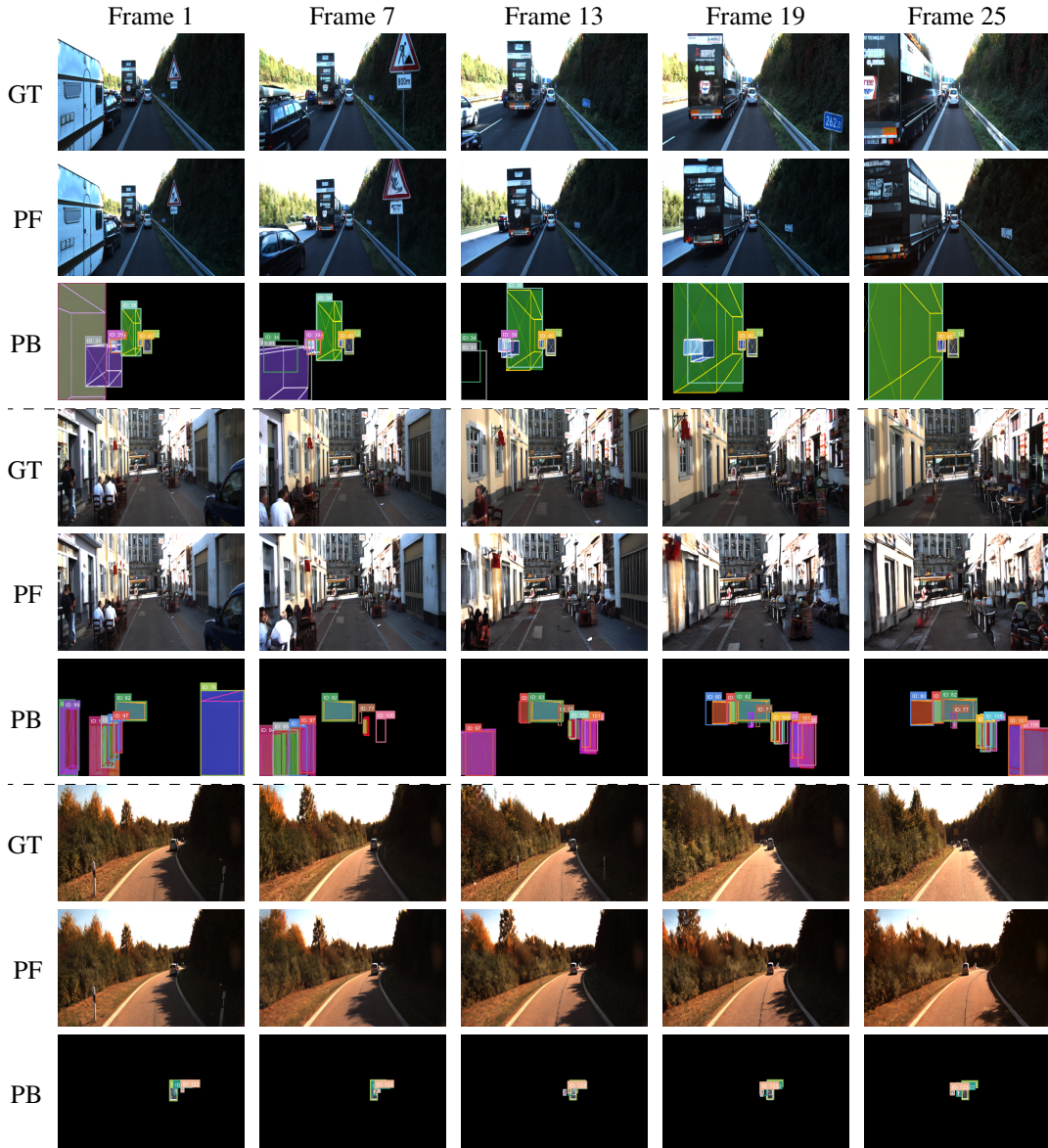


Figure 16: 3D bounding-box predictions and motion-controlled video generations for various scenes on KITTI test-split.

### C.5 Visualizing Motion Controlled Generation via Box2Video

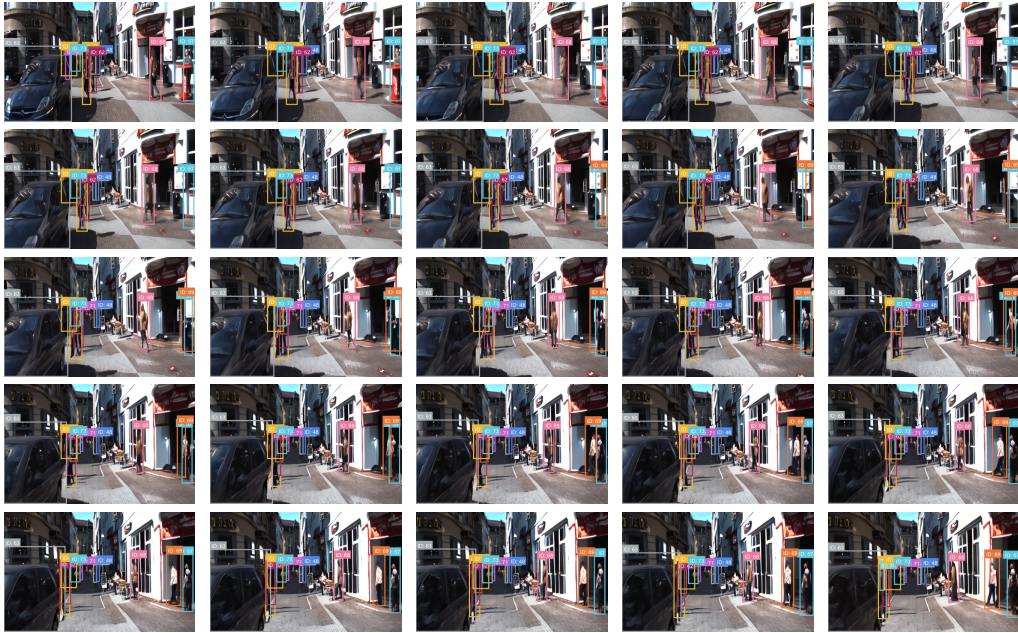


Figure 17: A frame-by-frame visualization of Box2Video generation, conditioned on the ground-truth bbox frame sequence from the KITTI dataset, with conditions outlined in the plots.



Figure 18: A frame-by-frame visualization of Box2Video generation, conditioned on the ground-truth bbox frame sequence from the vKITTI dataset. The ground-truth bboxes are outlined in the plots.



Figure 19: A frame-by-frame visualization of Box2Video generation, conditioned on the ground-truth bbox frame sequence from the BDD dataset. The ground-truth bounding boxes are outlined in the plots.

## D Key Insights and Future Directions

### D.1 Noteworthy Discoveries in our Box2Video Model

Our experiments have yielded findings suggesting that our Box2Video model not only understands bounding-box locations in scenes but also the encoded track IDs and 3D bounding-box orientation information in the rendered bounding-box frames. While these findings are not conclusive and require further investigation to be confirmed, they highlight potential directions for future projects. Here we share some of these findings to guide further research and development.

1. During preprocessing, we assign a random color to each track ID and fill the bounding boxes with their corresponding track IDs' colors. When our Box2Video receives unreasonable predictions, it still attempts to produce outputs that adhere to the given conditions, including the false bounding-box IDs.
2. In our 3D bounding box plots, we encode the vehicle's orientation by marking the rear end with an "X". Occasionally, our BBox Predictor incorrectly identifies the car's orientation, marking the front side with an "X". Therefore, during the video generation phase, we sometimes observe that the Box2Video model recognizes the wrong markings in the bounding box frames and generates a video of a car driving backwards.
3. We also observe that Box2Video may recognize the encoded object information regarding its class in the bounding box frames. Specifically, when an object is not present in the initial frame but its bounding box label appears in the final frame, the model can decode its class information and generate a correct instance of that class in the clip. However, we suspect that the object's class information could also be inferred from the bounding box shapes. Further investigation is required.
4. Given the previous findings, we believe that plotting the bounding-box outlines a bit thicker to make them more prominent could potentially improve our results.

### D.2 Future Directions

For future work, we believe it is worthwhile to develop a systematic approach to investigate the aforementioned observations. Additionally, it would be interesting to explore alternative methods for predicting bounding boxes. Furthermore, it would be beneficial to create a systematic method to measure the likelihood of the bounding box frames, instead of directly computing their IoU, recall, and precision rate with ground truth.